

2 THE CASE OF MAPbBr₃ VERSUS MAPbI₃

SUPPRESSION OF METHYLAMMONIUM MIGRATION AND REDUCTION OF HALIDE MIGRATION

Solar cells based on metal halide perovskites often show excellent efficiency but poor stability. This degradation of perovskite devices has been associated with the migration of mobile ions. MAPbBr₃ perovskite materials are significantly more stable under ambient conditions than MAPbI₃ perovskite materials. In this chapter, we use transient ion drift to quantify the key characteristics of ion migration in MAPbBr₃ perovskite solar cells. We then proceed to compare them with those of MAPbI₃ perovskite solar cells. We find that in MAPbBr₃, bromide migration is the main process at play and that contrary to the case of MAPbI₃, there is no evidence for methylammonium migration. Quantitatively, we find a reduced activation energy, a reduced diffusion coefficient, and a reduced concentration for halide ions in MAPbBr₃ compared to MAPbI₃. Understanding this difference in mobile ion migration is a crucial step in understanding the enhanced stability of MAPbBr₃ versus MAPbI₃.

This chapter is based on the following publication⁵⁶:
Lucie McGovern, Moritz H. Futscher, Loreta A. Muscarella and Bruno Ehrler, "Understanding the Stability of MAPbBr₃ versus MAPbI₃: Suppression of Methylammonium Migration and Reduction of Halide Migration", *Journal of Physical Chemistry Letters*, vol. 11, no. 17, pp. 7127–7132, 2020.

2.1 INTRODUCTION

Perovskite solar cells, with solution-based, cheap synthesis methods and a rapid increase in power conversion efficiency, are a promising candidate for future solar cells. Record efficiencies of 25.2 % and 29.2 % for single-junction and perovskite/silicon tandem configurations¹⁰ are already competitive with those of existing technologies. However, a major hurdle for commercialization remains, the degradation of high-efficiency perovskite materials under a range of environmental factors. Humidity^{57–59}, illumination^{60–63}, and thermal stress^{63,64} have all been shown to degrade the power conversion efficiency of the devices over time. Ion migration has been identified as one of the main drivers for degradation⁶⁵.

The stability of metal halide perovskites is composition-dependent. For example, MAPbI₃ is more sensitive to all of the environmental factors mentioned above than MAPbBr₃⁶⁶. Some mechanisms have been proposed to explain this stability enhancement. In terms of material degradation, decomposition studies link the enhanced stability of MAPbBr₃ to a predominance of the reversible decomposition reaction $\text{CH}_3\text{NH}_3\text{PbX}_3(\text{s}) \rightleftharpoons \text{CH}_3\text{NH}_2(\text{g}) + \text{HX}(\text{g}) + \text{PbX}_2(\text{s})$, compared to the irreversible decomposition pathway $\text{CH}_3\text{NH}_3\text{PbX}_3(\text{s}) \rightleftharpoons \text{NH}_3(\text{g}) + \text{CH}_3\text{X}(\text{g}) + \text{PbX}_2(\text{s})$, in contrast to MAPbI₃ that exhibits both types of decomposition⁶⁷. More recently, the decomposition reaction $4\text{CH}_3\text{NH}_3\text{PbX}_3 + \text{O}_2 \rightleftharpoons 4\text{PbX}_2 + 2\text{X}_2 + 2\text{H}_2\text{O} + 4\text{CH}_3\text{NH}_2$ has been shown to slow upon substitution of iodide with bromide⁶⁸.

In terms of ion migration, theoretical predictions for MAPbBr₃ suggest that the stronger Pb–Br bond^{69–72} could increase the halide ion defect formation energy⁷³ and thereby suppress the degradation caused by ion migration. Migration of the bulky MA⁺ ion might also be inhibited by steric hindrance, because the lattice constant of MAPbBr₃ is smaller^{74,75}, and/or by stronger hydrogen bonding to the surrounding Pb–Br₆ octahedra. However, though ion migration is one of the causes of degradation of perovskite devices⁶⁵, many of its aspects remain poorly understood. It is in fact unclear if the ion migration is reduced in MAPbBr₃ compared to MAPbI₃, and which aspect of the mobile ions is affected.

Here we use transient ion drift (TID) to quantify the characteristics of mobile ions in MAPbBr₃. We identify the nature of mobile ions and their

activation energy, concentration, and diffusion coefficients and compare them to the characteristics of mobile ions in MAPbI₃⁷⁶. We find that the concentration of mobile bromide ions is on average 8 times lower than in their iodide counterpart in MAPbI₃, and that the bromide ions diffuse ~ 3 times slower, with an activation energy that is slightly lower than that of the migration of iodide. Halide migration is therefore greatly affected when tuning the halide composition. However, the halide composition does not affect solely the halide migration, as one might expect. A striking difference between the iodide and bromide perovskites lies in the methylammonium (MA⁺) migration. We measure a high density of migrating MA⁺ ions in the iodide perovskite. In stark contrast, MA⁺ migration is inhibited in the bromide perovskite. This difference might be one of the keys to their higher structural stability, because the A-site cations have been shown to be critical for the structural properties of perovskites^{77,78}. We hence assign the higher stability of the MAPbBr₃ perovskite in part to slower and fewer mobile halide ions, and in part to the suppression of MA⁺ cation migration.

We use TID, a capacitance-based technique, to measure the mobile ions in the perovskite diodes. While there are several techniques for measuring ion migration, TID allows for discrimination between anion and cation migration and independently measures the number density (N_{ion}) and diffusion coefficient (D) of mobile ions. With temperature-dependent measurements of the capacitance transients, TID further quantifies the activation energy (E_a) for ions that migrate. A more detailed discussion of the technique can be found in reference [51].

2.2 RESULTS AND DISCUSSION

2.2.1 MAPbBr₃ SOLAR CELL DEVICE CONFIGURATION

We fabricate a full solar cell as the diode for capacitance measurements and choose suitable contact layers such that the main contribution to the ion drift comes from the perovskite layer. The architecture of the solar cell is a planar p-i-n junction as shown in Figure 2.1a. For a direct comparison with our reported results on MAPbI₃⁷⁶, we use the same transport layers: NiO_x as the hole transport layer and C₆₀ and BCP as electron transport layers. We also prepare the MAPbBr₃ perovskite using a similar antisolvent technique, modified slightly to yield films of similar thickness and grain size. Figure 2.1b shows a top view scanning electron microscopy (SEM) image of such a MAPbBr₃ perovskite film formed on

top of NiO_x. The film features a good surface coverage and an apparent grain size (as estimated by SEM morphology) between 200 and 500 nm, comparable to the average 300 nm size of MAPbI₃ perovskite grains from our previous report. Cross-sectional SEM shows layers of (180 ± 20) nm as shown in Figure 2.1c, also comparable to our MAPbI₃ solar cells. With MAPbBr₃, the device shows a power conversion efficiency of 2.7 % (Figure 2.1d), a value close to that of previous work with this simple architecture⁷⁹ (see Section 2.4.1). There is little hysteresis between the forward and reverse scans.

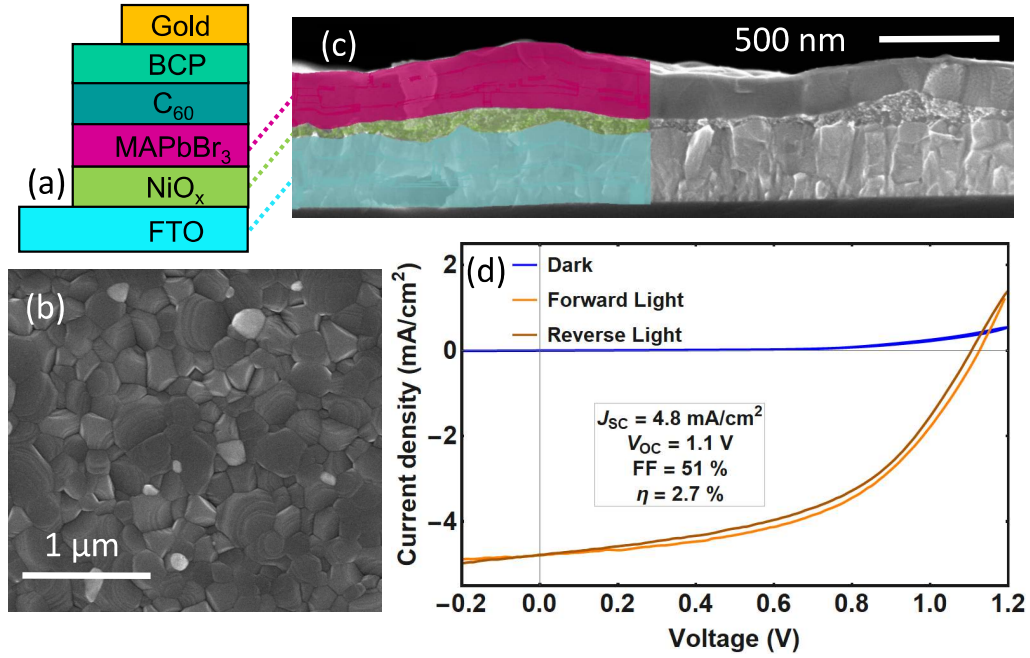


FIGURE 2.1. Inverted MAPbBr₃ device characteristics. (a) Solar cell architecture of the full device, with the MAPbBr₃ film sandwiched between a hole transport layer of NiO_x and an electron transport layer of C₆₀ and BCP. A fluoride tin oxide (FTO) bottom electrode and a gold top electrode complete the device, allowing for the extraction of the holes and electrons. (b) Top view SEM image of the MAPbBr₃ perovskite layer showing grains of 200 to 500 nm. (c) SEM cross-sectional image of the MAPbBr₃ perovskite layer on top of FTO and NiO_x. (d) Current–voltage characteristics measured in the dark and light, with a scan speed of 10 mV s⁻¹.

2.2.2 TID MEASUREMENT SHOWS BROMIDE MIGRATION IN MAPbBr₃

To measure the capacitance transients of the MAPbBr₃ solar cell device, we apply a voltage bias close to the built-in bias of the device (1.1 V) for 1 s to redistribute the ions. After the bias is released, the ions move back to the contacts and we record the resulting capacitance transients (Figure 2.2a; see Section S2.4.2 for experimental details). The relative capacitance change is presented in Figure 2.2b, with one transient every 10 K. We also repeat the whole measurement for a different filling voltage (1.4 V), as is presented in Figure 2.5.

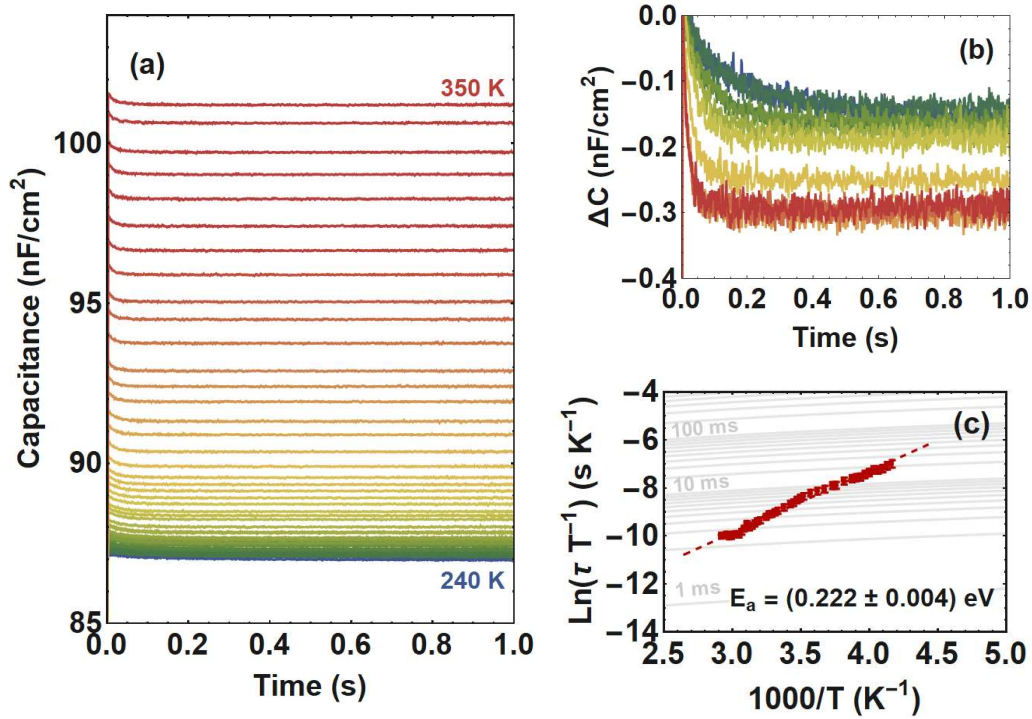


FIGURE 2.2. (a) Capacitance transient measurements of a MAPbBr₃ solar cell measured in the dark, with a DC voltage of 0 V and an AC voltage of 10 mV at 10^4 Hz, after applying a pulse of 1.1 V for 1 s. (b) Relative difference in capacitance $\Delta C = C(t) - C_{2.5 \text{ ms}}$ for the capacitance transients between 240 K and 340 K, in steps of 10 K. (c) Arrhenius plot showing the activation energy derived from this measurement.

The transients in panels a and b of Figure 2.2 show a small and rapid exponential decrease on the order of 10 ms, followed by a flat baseline when the system has reached its steady state. In TID of p-type semiconductors, we assign positive trends to the migration of cations and nega-

tive trends to the migration of anions. Hall measurements⁸⁰ suggest the p-type nature of MAPbBr₃. Additionally, both time-of-flight secondary ion mass spectroscopy (ToF-SIMS)⁸¹ and nanoprobe X-ray fluorescence (Nano-XRF)⁴² measure a time evolution of the spatial bromide concentration in MAPbBr₃ single crystals. We thus assign the negative feature present in the whole temperature range to bromide migration. As there is no apparent positive feature in the capacitance transients, we conclude that there is no or very little cation migration. If present at all, the mobile cation concentration must be below $1.5 \times 10^{13} \text{ cm}^{-3}$, the sensitivity threshold for this measurement (see Section 2.4.2). This is in contrast with our previous results for MAPbI₃, for which we found a combination of migration from the iodide (I⁻) anion and the MA⁺ cation⁷⁶, both with significant concentrations of mobile ions, $1 \times 10^{15} \text{ cm}^{-3}$ for I⁻ and $1 \times 10^{16} \text{ cm}^{-3}$ for MA⁺.

Substituting bromide for iodide in the MAPbX₃ (X = I or Br) framework thus leads to a significant suppression of MA⁺ migration. This effect was already hypothesized as a consequence of the structural contraction of the MAPbBr₃ framework⁶⁸ and/or the stronger hydrogen bonding between the lead halide octahedra and the MA⁺ cation^{68,82}. With regard to this second hypothesis, we note that although it has been evoked multiple times in the literature, the experimental data do not match but instead show an equal strength of hydrogen bonds whether using X = I, Br, or Cl in MAPbX₃^{83–85}. We therefore infer that the lattice contraction is the origin of the suppression of MA⁺ migration, an assessment that matches the trend found in density functional theory (DFT) modeling³⁴. This means that the lattice unit cell size makes a major contribution to the enhanced stability of these systems. This finding sheds light on the possible origin of the increased stability of complex mixed-cation/mixed-halide perovskites compared to pure-halide materials, as well as the origin of the higher stability of compressed perovskites. In the future, a systematic study of ion migration versus pressure could determine the specific compression factor, i.e., the specific unit cell size, necessary to suppress cation migration.

2.2.3 QUANTIFICATION OF BROMIDE MIGRATION CHARACTERISTICS

To quantify bromide migration, we fit each capacitance transient to extract τ , the lifetime of the process (see Section 2.4.2). Determined over many temperatures, the extracted lifetimes are used in an Arrhenius plot

Activation energy (eV)	Diffusion coefficient at 300 K (cm ² s ⁻¹)	Concentration of mobile ions (cm ⁻³)
(0.25 ± 0.05)	(8.4 ± 3.9) × 10 ⁻¹⁰	(1.3 ± 0.7) × 10 ¹⁴

TABLE I. Characteristics of mobile ions in MAPbBr₃ averaged from four individual measurements.

to obtain E_a and D , as shown in Figure 2.2c and Figure 2.5c. Using the Equation for mobile ion density (see Equation 2.5 in Section 2.4.2), N_{ion} is also measured. The results are listed in Table I, averaging over two different filling voltages each for two solar cells.

2.2.4 COMPARING ION MIGRATION PATTERNS IN MAPbBr₃ AND MAPbI₃

To understand the increased stability of MAPbBr₃ compared to that of MAPbI₃, we compare changes in ion migration (Figure 2.3). We have already presented the data for iodide migration in MAPbI₃ in previous work,⁽²¹⁾ and it is reproduced here for comparison.

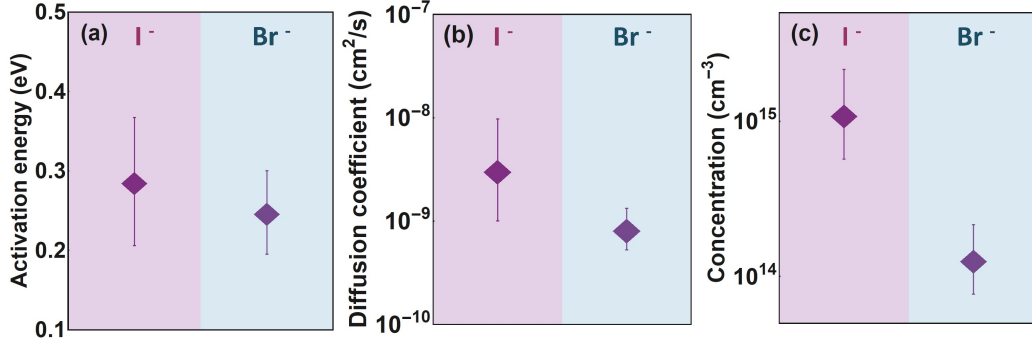


FIGURE 2.3. Comparison of mobile ions in MAPbBr₃ and MAPbI₃ showing (a) a reduced activation energy for bromide migration, (b) a reduced diffusion coefficient for bromide migration (at 300 K), and (c) a reduced density of bromide mobile ions. Error bars are the standard deviations of the weighted means.

Our initial hypothesis was an increase in the activation energy for bromide migration in MAPbBr₃, due to lead forming a stronger bond with bromide than iodide^{69–72}. Our results indicate the reverse trend, with an activation energy slightly decreasing from 0.29 eV for iodide migration to 0.25 eV for bromide migration. These values are close to experimental activation energies found by temperature-dependent hysteresis

measurements⁸⁶. We note that they differ, however, from DFT calculations by Lin *et al.*⁷³, a difference that may arise from the approximation their work uses, of a low-temperature phase with orthorhombic structure. The decrease in activation energy can potentially be rationalized by the smaller size of the bromide ion, possibly reducing the steric hindrance during the transition state of migration for bromide. Meggiolaro *et al.*³⁶ decompose the activation energy into the migration energy barrier $\Delta^\ddagger H^\circ$ and a DFE (defect formation energy) term, the latter accounting for the energy required to form the defect undergoing the jump. Using their finding that the lower limit for the DFE term to vanish is reached for ~ 250 nm grains, we can neglect DFE in our study. What these results serve to show is that the activation energy for ions to migrate is the result of an interplay of competing effects, in this case the steric hindrance versus the bond strength. These numbers can further help us to understand the halide migration mechanism. In fact, molecular dynamics (MD) modeling shows that in both MAPbI₃ and MAPbBr₃, the lowest activation energy for halide migration is through a vacancy-mediated hopping mechanism⁸⁶. The activation energies we measure are similar to the MD-simulated values, which helps us in elucidating the mechanism for halide migration in MAPbBr₃. A vacancy-mediated hopping pathway is likely dominating, as is the case in MAPbI₃^{33,37}.

We turn now to the comparison of the diffusion coefficients, which can be expressed through the following Equation⁵¹:

$$D = D_0 \exp\left(\frac{-\Delta^\ddagger G^\circ}{k_B T}\right) = \frac{v_0 d^2}{6} \exp\left(\frac{\Delta^\ddagger S^\circ}{k_B T}\right) \exp\left(\frac{-\Delta^\ddagger H^\circ}{k_B T}\right) \quad (2.1)$$

where $\Delta^\ddagger G^\circ$, $\Delta^\ddagger H^\circ$, and $\Delta^\ddagger S^\circ$ are the changes in Gibbs free energy, enthalpy, and entropy of activation, respectively, for a single ion migration step, k_B is the Boltzmann constant, v_0 is the attempt-to-escape frequency, and d is the jump distance. We choose to follow the usual formalism that refers to the change in Gibbs free enthalpy as activation energy E_a . We measure a bromide diffusion coefficient at 300 K of $\sim 1 \times 10^{-9} \text{ cm}^2 \text{ s}^{-1}$, 3 times less than that of iodide, at $3 \times 10^{-9} \text{ cm}^2 \text{ s}^{-1}$. Following Equation 2.1, if we combine a reduction in both the bromide diffusion coefficient $D(\text{Br})$ and the bromide activation energy $E_a(\text{Br})$, we find that either the attempt-to-escape frequency, $v_0(\text{Br})$, the jump distance, $d(\text{Br})$, or the entropy term, $\Delta S(\text{Br})$, must decrease compared to their iodide counterparts ($v_0(\text{I})$, $d(\text{I})$, and $\Delta S(\text{I})$). The jump distance $d(\text{Br})$ is probably shorter than $d(\text{I})$ due to the smaller lattice constant in

the bromide perovskite, with $[1.2 d(\text{Br})]^2 \simeq d(\text{I})^2$. However, this change is counterbalanced by the increase in the attempt-to-escape frequency $\nu_0(\text{Br})$, with $\nu_0(\text{Br}) \simeq 1.5 \nu_0(\text{I})$, a value that we derive from the Raman and FTIR blue-shifts when moving from iodide to bromide^{83,84,87}. This suggests that the entropy term decreases for bromide compared to iodide, i.e., that $\Delta S^\circ(\text{Br}) < \Delta S^\circ(\text{I})$. Solution calorimetry measurements^{15,16} for the perovskite formation reaction show that the enthalpic and entropic contributions are indeed of opposite directions for both MAPbI₃ and MAPbBr₃. Though of a different nature - the changes considered in references [15] and [16] are about the entropy and enthalpy of reaction and not the entropy and enthalpy of activation - these results underline the importance of considering not only the enthalpic contribution but also the entropic contribution in determining the ion migration diffusion coefficient. Taken together, this means that even if the activation energy to migrate is lower for a bromide ion than for an iodide ion, the reduced diffusion coefficient suggests a smaller entropic gain for bromide migration, explaining the overall trend.

The third element that TID allows us to quantify is the concentration of mobile bromide ions. Here we measure an average concentration of $1.3 \times 10^{14} \text{ cm}^{-3}$, i.e. 8 times lower than the average concentration of mobile iodide ions in MAPbI₃, at $1.1 \times 10^{15} \text{ cm}^{-3}$. The lower density of mobile bromide ions will reduce any ion-induced degradation in MAPbBr₃. This lower density probably results from an increase in the energy to form bromide vacancies, which in turn decreases the number of bromide vacancies and thus reduces the number of sites to which bromide ions can migrate.

It is worth mentioning that the concentrations found in the literature still differ by many orders of magnitude, mainly due to the differences in the models used to interpret experimental data⁸⁸ (see Section 2.4.2). The results reported here are consistent with various experimental studies^{53,89–92} that show ion concentrations between 10^{14} and 10^{16} cm^{-3} . Studies that report significantly higher ion concentrations typically assume a complete screening of the electric field in the perovskite⁹³.

Comparing ion migration in MAPbBr₃ and MAPbI₃ thus results in a smaller amount of slower mobile bromide ions, and a striking absence of methylammonium migration. The reduction in mobile ion concentration for MA⁺ is on the order of at least 10^3 , and on the order of 10 for X[−]. Taken together, these results suggest two independent mechanisms for the formation of either methylammonium or halide vacancies, or a combination of two independent mechanisms together with a joint mech-

anism, such as the one proposed by Walsh *et al.* for Schottky defects: $\text{nil} \rightarrow V'_{\text{MA}} + V^{\bullet}_{\text{X}} + \text{MAX}^{32}$. Inhibiting these defect formation reactions is thus essential for enhancing the stability of the MAPbBr₃ perovskite.

2.3 CONCLUSION

We use TID to provide a direct and reliable comparison of ion migration between MAPbBr₃ and MAPbI₃. Our finding is that the activation energy for bromide migration is reduced, contrary to simple bond strength considerations. Despite the reduced activation energy, the diffusion of halides is slower, presumably because of a lower entropic change for ion migration. We note that previously the focus has often been on activation energy when studying ion migration. We show that in addition to the activation energy, it is crucial to consider the entropy change during migration to understand the diffusion of mobile ions. We also find 8 times fewer halide ions migrating in MAPbBr₃ than in MAPbI₃, probably a consequence of the higher vacancy formation energy. Finally, we show that bromide substitution inhibits MA⁺ migration, due to lattice contraction. This suppression of A-cation migration enhances the structural stability of pure-halide perovskites and could be further used as a tool for stabilization of more complex and efficient mixed-cation mixed-halide perovskites.

2.4 APPENDIX

2.4.1 SOLAR CELL FABRICATION AND PERFORMANCE

DEVICE FABRICATION The device fabrication closely follows the one we have established for MAPbI₃ devices in reference [76]. Laser patterned fluoride tin oxide (FTO) glass substrates were cleaned by ultra-sonication for 20 minutes subsequently in detergent, deionized water, acetone, and isopropanol, followed by UV ozone treatment for 15 minutes. Nickel oxide (NiO_x) precursor solution (0.3 M nickel(II) acetylacetonate (Sigma Aldrich) in ethanol) filtered with PTFE 0.45 μm was spun on the cleaned FTO glass at 4000 rpm for 15 seconds, dried at 150 °C for 1 minute and then annealed with a slow heating rate of 3 °C/min until a temperature of 350 °C was reached. The samples were then left at 350 °C for 1 h.

The MAPbBr₃ perovskite precursor solution was prepared by dissolving 1.1 M of methylammonium bromide (MABr, TCI) and lead(II) bromide (PbBr₂, Sigma Aldrich) with 1:1 molar ratio into a 4:1 DMF (anhydrous, Aldrich):DMSO (anhydrous, Aldrich) solvent mix. The dissolution took place overnight on a hot plate at 60 °C. After having cooled, 100 μL of the MAPbBr₃ precursor solution was spun onto the NiO_x-coated substrates at 6000 rpm for 30 seconds in a nitrogen-filled glove box. 15 seconds after the beginning of the rotation, 100 μL of chlorobenzene anti-solvent (anhydrous, Aldrich) was quickly dropped onto the substrate. After the MAPbBr₃ spinning process, the substrates were annealed at 100 °C for 1 h. Following this, 30 nm of C₆₀ (0.2 Å s⁻¹ rate), 8 nm of bathocuproine (0.2 Å s⁻¹ rate) and 120 nm of gold (0.1 Å s⁻¹ for the first 10 nm, then 1.0 Å s⁻¹ for the remaining 110 nm) were deposited on top of the MAPbBr₃ layer by thermal sublimation at pressures below 8×10^{-6} mbar.

IMAGING OF DEVICE The SEM images were taken with a FEI Verios 460 scanning electron microscope in the secondary electron mode. An acceleration voltage of 10 kV and a working distance of 4 mm were used and field immersion mode was applied for an optimized resolution. To obtain the cross-section of the device, the sample was cleaved in the center.

SOLAR CELL PERFORMANCE The measured V_{OC} of 1.1 V (Figure 2.1d) is much lower than the 2.3 V perovskite bandgap⁹⁴, an effect which is commonly attributed to the mismatch between the energy levels of the MAPbBr₃ perovskite and the transport layers surrounding it. Indeed,

the valence band minimum of MAPbBr₃ (5.9 eV)⁹⁴ and the work function of the NiO_x HTL (5.2 eV)⁹⁵ have an energy difference of $\simeq 0.7$ eV, while the conduction band maximum of MAPbBr₃ (3.6 eV)⁹⁴ and the work function of the C₆₀ ETL (3.9 eV)⁹⁶ have an energy difference of $\simeq 0.3$ eV, amounting to a total loss of $\simeq 1.0$ eV. To counteract this discrepancy, some groups have put efforts in the modification and engineering of interfaces leading to promising V_{OC}s above 1.6 eV⁷⁹. Such interfaces are an important pathway towards optimized devices but here they would prevent a direct one-to-one comparison with our previously reported MAPbI₃ solar cell.

2.4.2 CAPACITANCE MEASUREMENTS

GENERAL CONSIDERATIONS To avoid air exposure, the sample was loaded into a Janis VPF-100 liquid nitrogen cryostat inside a nitrogen-filled glovebox. Current-voltage, impedance spectroscopy, capacitance-voltage, and transient ion-drift measurements were performed at a pressure below 2×10^{-6} mbar, in the dark, using a commercially available DLTS system from Semetrol. To ensure thermal equilibrium, the temperature of the sample was held constant for at least 30 minutes before current-voltage, impedance spectroscopy, and capacitance-voltage measurements. The capacitance was modelled by a capacitor in parallel with a conductance. Capacitance transient measurements were performed from 240 K to 340 K in steps of 2 K with a temperature accuracy of 0.2 K. The sample was held at 240 K for 30 minutes before starting the transient ion-drift measurement.

IMPEDANCE AND MOTT-SCHOTTKY ANALYSIS To perform the TID measurement, we need to properly select the frequency of the AC voltage used to measure capacitance. To do so, we measure the impedance spectrum of our device. As seen in Figure 2.4a, the impedance shows three different regimes: at high frequencies (in this case above 10^5 Hz) the capacitance is limited by the series resistance of the device. At intermediate frequencies (in Figure 2.4a between 10^2 Hz and 10^4 Hz for the capacitance taken at 240 K) lies a plateau where the capacitance is determined by the depletion capacitance, here approximated to a parallel plate capacitor. The discontinuities stem from changes in the resistor over which the capacitance is measured. At low frequencies (in Figure 2.4a below 10^2 Hz for the 240 K capacitance) an additional component arises, and the measured capacitance increases in a fashion that is dependent on the temperature, a phenomenon linked to ion accumulation

at the interfaces^{54,55,89,91,97}. To perform our TID measurement, we thus choose a frequency of 10^4 Hz, in the intermediate frequency regime, where the measured capacitance is influenced neither by ion accumulation nor series resistance.

When measuring TID, we apply a voltage bias to collapse the depletion layer in the perovskite. In order to fully collapse the depletion layer, this voltage bias should be close to the built-in voltage V_{BI} . We determine V_{BI} through Mott-Schottky analysis using the following Equation, where A is the area of the capacitor.

$$\Delta C = A \sqrt{\frac{q \epsilon_0 \epsilon N_D}{2 (V_{BI} - V)}} \quad (2.2)$$

In a Mott-Schottky plot, the inverse squared of the capacitance is plotted against voltage. The linear regime of the curve is fitted, then V_{BI} is the intercept of this fit with the x-axis. Figure 2.4b shows a V_{BI} of 1.3 eV for this solar cell architecture. We thus apply voltage pulses of 1.1 V and 1.4 V in our subsequent TID measurements. Two other parameters can be extracted from a Mott-Schottky plot: the density of electronic doping N_D , and the perovskite permittivity ϵ . Similar to our TID assumption, we assume again that the mobile ion density is smaller than the electronic doping density, such that the ions only pose a small perturbation. Within this framework, the electronic doping density N_D evolves with the applied voltage and is thus determined by the slope of the Mott-Schottky curve. On the contrary, at full depletion the perovskite permittivity ϵ does not evolve with the applied voltage, and is thus extracted from the capacitance value in the plateau regime, in our case at 0 V. The results for N_D and ϵ are given in the inset of Figure 2.4b. These values are used for solving Equation 2.4 and Equation 2.5. We note that this Mott-Schottky analysis assumes the validity of the depletion approximation for the perovskite solar cells measured⁹⁸. Indeed two slopes appear in the Mott-Schottky plot, one related to the depletion capacitance, the second to the chemical capacitance, due to charge-carrier injection at high forward biases. By considering only the slope at intermediate forward bias, we make sure we measure the depletion capacitance.

TRANSIENT ION DRIFT Three key parameters can be quantified by TID: the activation energy for ions to migrate, E_a , the ion diffusion coefficient prefactor, D_0 , and the mobile ion concentration, N_{ion} .

These can be extracted using the following set of equations, where

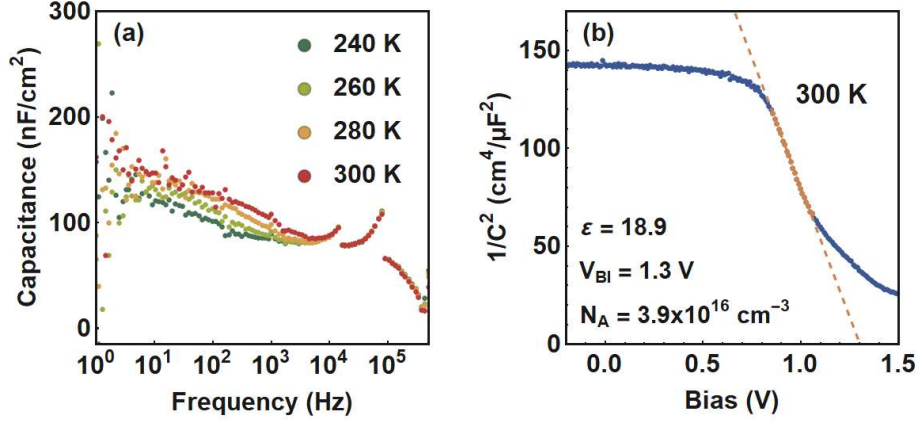


FIGURE 2.4. (a) Impedance spectroscopy measured in the dark at 0 V with an AC perturbation of 10 mV, (b) Mott-Schottky characteristics measured at 300 K in the dark with an AC perturbation of 10 mV at 10⁴ Hz.

$C(\infty)$ is the capacitance at steady-state, C_0 is the initial capacitance at time $t = 0$ after releasing the voltage pulse, ΔC is the magnitude of the transient, ϵ_0 is the vacuum permittivity, ϵ is the perovskite permittivity, q is the electric charge, and N_D is the electronic doping density. The assumptions of the model are detailed in Chapter 1.

$$C(t) = C(\infty) \pm \Delta C \exp\left(\frac{-t}{\tau}\right) \quad (2.3)$$

$$\tau = \frac{k_B T \epsilon_0 \epsilon}{q^2 D_0 N_D} \exp\left(\frac{E_a}{k_B T}\right) \quad (2.4)$$

$$\Delta C = C(\infty) - C_0 = C(\infty) \frac{N_{ion}}{2 N_D} \quad (2.5)$$

The fitting procedure goes as follows. To obtain the time constants for ion migration, each capacitance transient is fitted individually with a function containing between one and four exponential decay components. Within our chosen confidence level (p value > 0.05), most capacitance transients are fitted with a mono-exponential decay. These are shown in red in Figure 2.2 and in Figure 2.5. The obtained values for E_a , D_0 , and N_{ion} and their error bars are presented in Table I and Figure 2.3. The errors are calculated using the standard deviation of four measurements, each weighed by the error on its fit.

We note that the values presented in Table I in Section 2.2.3 are calculated under the assumption that the perovskite permittivity is

temperature-independent in the range considered, using the value found at 300 K. We also note that our values for the perovskite permittivity follow a similar trend to previous works^{99–103}, with an almost constant value from 240 K to 300 K as apparent from the almost constant capacitance at long times, see Figure 2.5. This assumption might, however, break for temperatures above 300 K. If we assume instead a temperature-dependent perovskite permittivity calculated from the steady-state capacitance, we find only small changes in the extracted values, where the activation energy changes from (0.25 ± 0.05) eV to (0.26 ± 0.10) eV, and the diffusion coefficient from $(8.4 \pm 3.9) \times 10^{-10} \text{ cm}^2\text{s}^{-1}$ to $(8.7 \pm 4.2) \times 10^{-10} \text{ cm}^2\text{s}^{-1}$.

We use Equation 2.5 to estimate the minimum sensitivity threshold to detect a migrating species, with $N_{ion}(min) = \frac{\Delta C}{C(\infty)} \times 2N_D \simeq 3.7 \times 10^{-4} \times 2N_D \text{ cm}^{-3}$. Below this value – i.e. in this study below $1.5 \times 10^{13} \text{ cm}^{-3}$ – we are unable to detect a mobile ionic species. We would further not be able to detect an ionic species with a positive charge if it had a very similar activation energy and diffusion constant as the negative feature. The combination of these factors is highly unlikely, and we thus conclude that there is probably no mobile positively charged ion with a density above $1.5 \times 10^{13} \text{ cm}^{-3}$.

While fitting the data, we notice a discontinuity in the very first points measured, before the expected exponential decay arises. We hypothesize this effect to be due to a circuit overload in the first milliseconds. In our subsequent fitting procedure, we thus use the data from time 2.5 ms (point number 7 of the measurement) to time 1 s (point number 2042).

For a few filling voltages, the high-temperature fits do not match the Arrhenius trend. These fitted values are shown in blue in Figure 2.5. The component is slow ($50 \text{ ms} < \tau < 200 \text{ ms}$) and of low amplitude such that we are not able to assign an activation energy to this process. Because these arise only at high temperatures, and mostly at higher filling voltages, we hypothesize a reversible interfacial effect between the perovskite layer and the contact layers.

CAPACITANCE TRANSIENTS AND ARRHENIUS PLOT FOR A FILLING VOLTAGE OF 1.4 V In Figure 2.5 below, we show the capacitance transients and the Arrhenius plot for a MAPbBr₃ solar cell measured after applying a filling bias of 1.4 V for 1 s (as opposed to 1.1 V in Figure 2.2). From the Arrhenius plot, we extract the activation energy for the migration step $E_a = 0.220 \pm 0.05 \text{ eV}$, and find that this value is equivalent to the one obtained when applying the 1.1 V filling bias, where

$$E_a = 0.222 \pm 0.04 \text{ eV}.$$

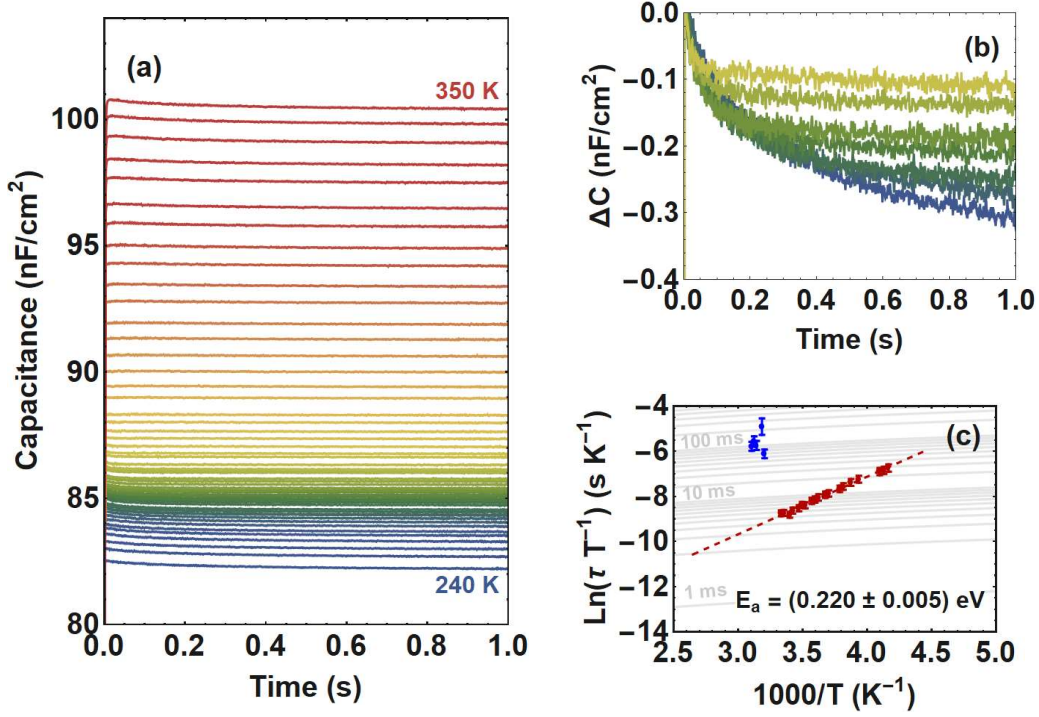


FIGURE 2.5. (a) Capacitance transient measurements of a MAPbBr₃ solar cell measured in the dark, with a DC voltage of 0 V and an AC voltage of 10 mV at 10⁴ Hz, after applying a pulse of 1.4 V for 1 s. (b) Relative difference in capacitance $\Delta C = C(t) - C_{2.5 \text{ ms}}$ for the capacitance transients between 240 K and 300 K. (c) Arrhenius plot showing the activation energy derived from this measurement, in red. In blue are the high-energy temperature points that we associate to a reversible interfacial effect between the perovskite and the contact layers.